

Accuracy of atmospheric parameters of FGK dwarfs determined by spectrum fitting

T. Ryabchikova^{1*}, N. Piskunov², Yu. Pakhomov¹, V. Tsymbal³, A. Titarenko^{1,4},
T. Sitnova^{1,4}, S. Alexeeva¹, L. Fossati⁵, L. Mashonkina¹

¹*Institute of Astronomy, Russian Academy of Sciences, Pyatnitskaya 48, 119017 Moscow, Russia*

²*Department of Physics and Astronomy, Division of Astronomy and Space Physics, Uppsala University, Box 516, 751 20 Uppsala, Sweden*

³*Physical Technical Institute, Crimean Federal University, Vernadskiy's Avenue 4, 95007 Simferopol, Crimea*

⁴*Department of Astronomy, Physics Faculty, M.V.Lomonosov Moscow State University, GSP-1, 1-2 Leninskye Gory, 119991 Moscow, Russia*

⁵*Space Research Institute, Austrian Academy of Sciences, Schmiedlstrasse 6, A-8042 Graz, Austria*

Accepted XXX. Received YYY; in original form ZZZ

ABSTRACT

We performed extensive tests of the accuracy of atmospheric parameter determination for FGK stars based on the spectrum fitting procedure Spectroscopy Made Easy (SME). Our stellar sample consists of 13 objects, including the Sun, in the temperature range 5000–6600 K and metallicity range -1.4 – $+0.4$. The analysed stars have the advantage of having parameters derived by interferometry. For each star we use spectra obtained with different spectrographs and different signal-to-noise ratios (S/N). For the fitting we adopted three different sets of constraints and test how the derived parameters depend upon the spectral regions (masks) used in SME. We developed and implemented in SME a new method for estimating uncertainties in the resulting parameters based on fitting residuals, partial derivatives, and data uncertainties. For stars in the 5700–6600 K range the best agreement with the effective temperatures derived by interferometry is achieved when spectrum fitting includes the H α and H β lines, while for cooler stars the choice of the mask does not affect the results. The derived atmospheric parameters do not strongly depend on spectral resolution and S/N of the observations, while the uncertainties in temperature and surface gravity increase with increasing effective temperature, with minima at 50 K in T_{eff} and 0.1 dex in $\log g$, for spectra with S/N=150–200. A NLTE analysis of the Ti I/Ti II and Fe I/Fe II ionisation equilibria and abundances determined from the atomic C I (NLTE) and molecular CH species supports the parameters we derived with SME by fitting the observed spectra including the hydrogen lines.

Key words: stars: fundamental parameters – stars: abundances – methods: observational – methods: data analysis – stars: individual: Procyon, HD 49933, ν And, β Vir, HD 149026, HD 209458, Sun, HD 1461, 61 Vir, HD 69830, HD 189733, δ Eri, HD 103095

1 INTRODUCTION

The discovery of exoplanets, the results of the Kepler space mission, and the expected huge amount of information from the Gaia mission have attracted special attention to the problem of accurately determining atmospheric parameters for a large number of stars. Accurate atmospheric parameters are essential for exoplanet studies to best derive the planet parameters (e.g., mass, radius, and equilibrium temperature) and to characterise their atmospheres. The Gaia

mission¹ will provide unprecedented positional and proper motion measurements for about one billion stars in our Galaxy and throughout the Local Group and, thus, accurate parallaxes needed to improve stellar surface gravities. Accurate kinematic properties together with accurate atmospheric parameters will allow one to constrain Galactic stellar populations and chemical evolution more accurately than ever been possible before. This space mission is supported by ground-based spectroscopic observations within the Gaia-ESO Survey (GES) project (Gilmore et al. 2012). Determi-

* E-mail: ryabchik@inasan.ru

¹ <http://sci.esa.int/gaia/>

nation of atmospheric parameters for the GES benchmark and program stars was discussed by Smiljanic et al. (2014) and Heiter et al. (2015).

Determining atmospheric parameters for a large number of stars requires the development of automatic procedures capable of quickly producing reliable results. Following this reasoning, several different automatic spectral analysis procedures were developed during the last decades. All of them are essentially based on either the fit of synthetic to observed spectra or the measurement and analysis of equivalent widths (*EW*) of metal lines. For F-, G-, and K-type stars and for both techniques various authors claimed a very high accuracy of the order of 20–40 K in effective temperature, 0.02–0.06 dex in surface gravity, and 0.02–0.05 dex in metallicity derived in the spectral analysis with $S/N \sim 150$ –400 (Valenti & Fischer 2005; Sousa et al. 2006). Nevertheless, it has been shown that analysis of the spectra obtained using the same spectrograph, but in different observational runs may lead to results that differ in effective temperature by 70 K, though the spectra had been analysed using the same technique (e.g., see Table 3 of Gonzalez et al. 2010). The situation is getting worse, when analysing the same spectra with different techniques. Torres et al. (2012) compared atmospheric parameters derived by the spectrum fitting and the *EW* techniques, and for stars hotter than 6000 K they found that the values from the spectrum fitting method are systematically lower compared to those from the *EW* method. Smiljanic et al. (2014) showed the presence of a large spread in the atmospheric parameters derived by thirteen different groups using different techniques for 11 bright F-, G-, and K-type main-sequence stars (the Gaia FGK benchmark stars). The Gaia spectral library collects spectra for these stars (Blanco-Cuaresma et al. 2014). Most of them have $S/N > 200$. The average difference between the recommended effective temperatures and gravities and individual determinations from the six different spectrum fitting and seven *EW* methods ranges between 46 K and 186 K and 0.09 dex and 0.28 dex, respectively. The largest discrepancies are probably caused by a systematic component, which is usually difficult to accurately estimate. It is worth noting, the difference in parameters reaches 100 K in effective temperature and 0.16 dex in surface gravity even between the two groups using a common technique based on *EW*. The analysis of the results for all groups of FGK dwarfs led to a method-to-method dispersion of ± 150 K in T_{eff} , ± 0.30 dex in $\log g$, and ± 0.10 dex in $[\text{Fe}/\text{H}]$. The situation is even worse for giant and metal-poor stars. These examples show how far the actual uncertainties may differ from the adopted ones.

This paper presents an extensive analysis of the uncertainties in atmospheric parameter determination made with the fitting procedure Spectroscopy Made Easy (SME, Valenti & Piskunov 1996). The investigated stars and their spectra are described in Section 2. A short description of the SME tool, the implemented modifications, and the error analysis are given in Section 3. We tested the best recommended atmospheric parameters and their uncertainties in Section 5 by inspecting the Ti I/Ti II and Fe I/Fe II ionisation equilibrium and element abundances from the atomic C I and molecular CH lines. Section 6 summarises our conclusions.

2 OBSERVATIONS

For the spectroscopic analysis we choose the 13 main-sequence (MS) stars including the Sun (Table 1) in the 4900–6600 K temperature range and with metallicity between $[\text{Fe}/\text{H}] = -1.5$ and $+0.3$ dex. All the stars, except HD 149026, have, at least, one interferometric determination of radius and effective temperature. Our methods of atmospheric parameter determination were first applied to the Sun that is the only star with a directly measured effective temperature and surface gravity.

Spectra of the program stars were obtained with different spectrographs. Most data were extracted from the following archives: the UVES/VLT and HARPS/3.6 m spectrographs at ESO², the ELODIE/1.93-m spectrograph³ at the Observatoire de Haute Provence, and the ESPaDONs spectrograph at the Canada-France-Hawaii Telescope⁴ (CFHT). Spectra of β Vir and HD 103095 were obtained with the FOCES spectrograph at 2.2-m telescope of the Calar Alto Observatory (Fuhrmann 1998). One of the spectra of 61 Vir was obtained with the Hamilton Echelle Spectrograph attached to the Shane 3-m telescope of the Lick Observatory (Sitnova et al. 2015). Spectra of few stars, including that of the Sun reflected from Ganymede, were obtained with the HiReS/Keck spectrograph (Howard et al. 2010). All the retrieved spectra have been reduced with the standard reduction pipelines available for each spectrograph. For the Sun, we used the National Solar Observatory (NSO) solar flux spectrum (Kurucz et al. 1984).

For each star we tried to find an archival spectrum with as high as possible signal-to-noise ratio (S/N). All observed spectra have a resolving power $R > 40\,000$ with a peak resolution of $R \sim 110\,000$ obtained with the UVES and HARPS spectrographs. Most ESPaDONs spectra have been collected in spectropolarimetric mode, which provides spectra with a resolution of $R = 65\,000$ instead of $R = 80\,000$ reached with the “object only” mode. Rather large range of S/N and R for the collected spectra allows us to thoroughly explore the uncertainties in the atmospheric parameters as a function of the basic spectral characteristics. Detailed information on the spectral resolution and S/N along with the program ID is given in Table 1 for each analysed spectrum. Continuum rectification was performed using low-order polynomials, giving special attention to the regions covered by the H β and H α lines, which play a crucial role in the atmospheric parameter determination.

3 ATMOSPHERIC PARAMETER DETERMINATION

We determined the stellar atmospheric parameters with the SME package (Valenti & Piskunov 1996). The tool SME was designed to perform an analysis of stellar spectra using spectrum fitting techniques in a consistent and reproducible way. The fit can be done in several spectral intervals simultaneously. The data points can further be masked to avoid observational defects and/or spectral regions with uncertain

² http://archive.eso.org/eso/eso_archive_main.html

³ <http://atlas.obs-hp.fr/elodie/>

⁴ <http://www.cadc-ccda.hia-ihp.nrc-cnrc.gc.ca/en/cfht/>

Table 1: List of investigated stars and spectrographs used to collect the spectra. The first column lists also the resolving power of each spectrum. Column 2 gives the average S/N calculated in the three wavelength ranges discussed in Sect. 3.1. The atmospheric parameters derived with SME are given in columns 4, 5, and 6, while columns 7 and 8 list the atmospheric parameters derived from interferometry. The last four columns indicate the spectroscopic atmospheric parameters from the literature and their source. The uncertainties are given in parentheses.

Observations		SME				Interferometry			Other spectroscopy			
Spectrograph	S/N	mask	T_{eff}, K	$\log g$	[M/H]	T_{eff}, K	$\log g$	Reference	T_{eff}, K	$\log g$	[M/H]	Reference
Resol. power												
Program ID												
(1)	(2)	(3)	(4)	(5)	(6)	(7)	(8)	(9)	(10)	(11)	(12)	(13)
HD 61421 = Procyon												
UVES	500	m6	6615(89)	3.89(33)	-0.05(05)	6597(18)	4.00(02)	Boyajian et al. (2013)	6485(80)	3.89(09)	0.01(07)	Bruntt et al. (2010)
(80000)		m5	6579(93)	3.84(37)	-0.07(05)	6573(42)	4.00(02)	Boyajian et al. (2013)	6593(50)	3.90(01)	0.02(03)	Gonzalez et al. (2010)
UVES POP		m4	6690(89)	3.85(25)	-0.02(05)	6563(33)	4.00(02)	Boyajian et al. (2013)	6660(95)	4.05(06)	0.02(09)	Doyle et al. (2013)
(Bagnulo et al. 2003)		VF	6602(112)	3.98(17)	-0.11(07)	6562(32)	4.00(02)	Boyajian et al. (2013)				
HD 49933												
HARPS	350	m6	6582(115)	4.00(52)	-0.48(09)	6635(90)	4.21(05)	Boyajian et al. (2013)	6570(60)	4.28(06)	-0.44(03)	Bruntt (2009)
(110000)		m4	6653(143)	4.08(33)	-0.44(08)				6600(80)	4.15(05)	-0.47(07)	Sitnova et al. (2015)
076.C-0279		VF	6512(120)	4.13(20)	-0.57(10)							
ESPaDONs	300	m6	6546(100)	4.04(52)	-0.50(08)							
(65000)		m4	6706(149)	4.22(33)	-0.41(08)							
05bf6a		VF	6567(107)	4.17(15)	-0.54(08)							
HD 9826 = ν And												
ESPaDONs	700	m6	6145(39)	4.06(12)	0.05(02)	6177(25)	4.13(03)	Boyajian et al. (2013)	6170(48)	4.00(08)	0.08(04)	Gonzalez et al. (2010)
(65000)		m4	6323(38)	4.25(12)	0.15(03)	6027(26)	4.10(02)	Boyajian et al. (2013)	6239(37)	4.19(03)	0.14(03)	Gonzalez et al. (2010)
05BO2		VF	6292(27)	4.22(04)	0.07(03)							
ELODIE	250	m6	6132(84)	4.03(30)	0.14(06)							
(42000)												
HiReS	200	m4	6354(103)	4.33(28)	0.13(07)							
(69000)		VF	6278(76)	4.20(09)	0.08(07)							
HD 102870 = β Vir												
ESPaDONs	1000	m6	6122(27)	4.07(10)	0.10(02)	6054(13)	4.11(04)	Boyajian et al. (2013)	6050(80)	3.98(07)	0.12(07)	Bruntt et al. (2010)
(65000)		m4	6232(27)	4.18(09)	0.18(02)				6111(28)	4.00(05)	0.16(02)	Gonzalez et al. (2010)
05bf6a		VF	6214(21)	4.13(03)	0.12(02)				6180(36)	4.15(05)	0.21(03)	Gonzalez et al. (2010)
FOCES	250	m6	6122(85)	4.02(30)	0.13(11)				6170(80)	4.14(04)	0.11(06)	Sitnova et al. (2015)
(60000)		m4	6242(81)	4.14(23)	0.21(06)							
		VF	6218(75)	4.10(13)	0.14(04)							

Table 1: continue.

(1)	(2)	(3)	(4)	(5)	(6)	(7)	(8)	(9)	(10)	(11)	(12)	(13)
HD 149026												
ESPaDONs	200 m6		6074(82)	4.18(29)	0.24(06)				6131(35)	4.22(05)	0.31(03)	Gonzalez et al. (2010)
(65000)	m4		6239(74)	4.33(23)	0.33(06)				6103(66)	4.27(05)	0.24(07)	Torres et al. (2012)
07ah28a	VF		6183(62)	4.22(09)	0.27(05)							
HiReS	300 m4		6285(95)	4.46(31)	0.37(07)							
(69000)	VF		6137(85)	4.23(17)	0.28(07)							
HD 209458												
ESPaDONs	1250 m6		6033(28)	4.28(08)	-0.05(02)	6092(103)	4.28(10)	Boyajian et al. (2015)	6118(25)	4.50(04)	0.03(02)	Sousa et al. (2008)
(80000)	m4		6160(27)	4.39(07)	0.02(07)				6117(26)	4.48(08)	0.02(03)	Santos et al. (2004)
co-added ⁵	VF		6145(15)	4.41(02)	-0.05(02)							
			6065(50)	4.42(04)	0.00(05)	Torres et al. (2008)						
HARPS	300 m6		6010(74)	4.23(22)	-0.08(05)							
(110000)	m4		6116(65)	4.35(16)	-0.01(04)							
co-added ⁶	VF		6112(45)	4.38(06)	-0.07(04)							
UVES	300 m6		5987(70)	4.25(23)	-0.09(05)							
(110000)	m4		6106(67)	4.38(17)	-0.02(05)							
co-added ⁷	VF		6093(42)	4.38(06)	-0.07(04)							
HiReS	170 m4		6174(140)	4.43(39)	0.02(10)							
(69000)	VF		6181(103)	4.42(18)	-0.03(08)							
ELODIE	170 m6		5980(123)	4.19(40)	-0.08(09)							
(42000)	m4		6152(120)	4.36(33)	0.02(09)							
Sun												
Atlas	1000 m6		5757(24)	4.41(06)	-0.03(02)	5777	4.44					
(550000)	m4		5787(22)	4.44(05)	-0.01(02)							
	VF		5773(12)	4.41(02)	-0.06(02)							
HiRes	200 m4		5778(67)	4.43(18)	-0.00(06)							
(69000)	VF		5792(42)	4.46(06)	-0.06(04)							
HD 1461												
UVES	270 m6		5732(55)	4.31(17)	0.14(05)	5386(60)	4.23(05)	von Braun et al. (2014)	5765(18)	4.38(03)	0.19(01)	Sousa et al. (2008)
(115000)	m4		5764(51)	4.35(16)	0.16(04)				5751(50)	4.33(07)	0.18(04)	Ramírez et al. (2009)
076.B-0055	VF		5798(38)	4.36(06)	0.13(04)				5765(44)	4.41(06)	0.18(03)	Valenti & Fischer (2005)
HiRes	150 m4		5805(80)	4.41(23)	0.18(07)							
(69000)	VF		5837(53)	4.40(09)	0.16(06)							
ELODIE	150 m6		5757(92)	4.31(28)	0.12(08)							

⁵ 05BC16, 05BH32A, 06AC12, 06AH20A⁶ 076.C-0878, 183.C-0972, 074.C-0012, 60.A-9036⁷ 265.C-5038, 067.C-0206, 077.C-0379, 087.D-0010, 088.C-0879

Table 1: continue.

(1)	(2)	(3)	(4)	(5)	(6)	(7)	(8)	(9)	(10)	(11)	(12)	(13)
(42000)		m4	5815(89)	4.36(25)	0.17(08)							
HD 115617 = 61 Vir												
ESPaDONs	700	m6	5567(27)	4.42(07)	-0.03(02)	5538(13)	4.42(03)	von Braun et al. (2014)	5558(19)	4.36(03)	-0.02(01)	Sousa et al. (2008)
(65000)		m4	5595(23)	4.45(06)	-0.01(02)				5490(80)	4.40(12)	-0.10(05)	Sitnova et al. (2015)
11AC04		VF	5588(12)	4.46(02)	-0.06(02)							
Lick	200	m4	5559(69)	4.42(18)	-0.02(06)							
(60000)		VF	5617(54)	4.45(09)	0.02(07)							
HD 69830												
ESPaDONs	650	m6	5422(43)	4.47(12)	-0.04(04)	5394(62)	4.46(04)	Tanner et al. (2015)	5402(28)	4.40(04)	-0.06(02)	Sousa et al. (2008)
(65000)		m4	5436(39)	4.49(10)	-0.03(04)				5413(28)	4.52(07)	-0.01(02)	Gonzalez et al. (2010)
14AF14		VF	5419(23)	4.48(05)	-0.09(04)				5382(25)	4.34(09)	-0.02(02)	Gonzalez et al. (2010)
HiRes	200	m4	5424(60)	4.58(17)	0.04(07)				5385(20)	4.37(02)	-0.05(02)	Sousa et al. (2006)
(69000)		VF	5415(45)	4.49(10)	-0.09(07)							
HD 189733												
ESPaDONs	1500	m6	5049(10)	4.53(03)	-0.02(01)	4875(43)	4.56(03)	Boyajian et al. (2015)	5051(47)	4.53(08)	-0.03(05)	Sousa et al. (2006)
(65000)		m4	5076(8)	4.58(03)	-0.00(01)				5111(77)	4.59(01)	-0.04(07)	Torres et al. (2012)
co-added ⁸		VF	5016(6)	4.64(02)	-0.05(01)				5034(90)	4.54(10)	-0.03(07)	Fuhrmann (2008)
HiRes	180	m4	5056(68)	4.53(18)	-0.02(10)				4952(64)	4.26(12)	0.01(04)	Gonzalez et al. (2010)
(69000)		VF	5019(62)	4.57(16)	-0.06(09)							
HD 23249 = δ Eri												
HARPS	500	m5	5040(28)	3.73(07)	0.05(03)	4955(30)	3.77(03)	Boyajian et al. (2013)	5150(51)	3.89(08)	0.13(04)	Sousa et al. (2008)
(110000)		m4	5037(21)	3.73(06)	0.05(02)				5015(80)	3.77(05)	0.15(07)	Bruntt et al. (2010)
60.A-9036		VF	5053(15)	3.87(05)	0.05(03)							
HiRes	200	m4	5052(48)	3.76(14)	0.07(06)							
(69000)		VF	5085(27)	3.78(07)	0.05(05)							
HD 103095												
FOCES	150	m6	4958(46)	4.52(17)	-1.38(10)	4771(18)	4.56(03)	Boyajian et al. (2013)	5130(65)	4.66(06)	-1.26(08)	Sitnova et al. (2015)
(60000)		m4	4944(43)	4.48(15)	-1.36(09)	4831(25)	4.58(04)	Boyajian et al. (2013)	5110(80)	4.66(10)	-1.35(05)	Fuhrmann (1998)
		VF	4904(27)	4.49(07)	-1.52(06)				4930(44)	4.65(06)	-1.37(03)	Valenti & Fischer (2005)

⁸ 06AF34, 06bd01, 06bf27, 07AC27

atomic/molecular data. Since the first version of SME, a number of modifications and improvements were made to the original version. They include new molecular and negative hydrogen ion partition functions and equilibrium constants in the equation-of-state (EOS) package, a new algorithm for solving the radiative transfer (the Feautrier algorithm was replaced with a Bezier attenuation operator scheme; see de la Cruz Rodríguez & Piskunov 2013), and a modification of the interpolation procedure in the model atmosphere grid. Further details of the current version of SME can be found in the upcoming paper by Piskunov & Valenti (2015). In this work, we use the `sme_443` package version. The SME package is working with various grids of model atmospheres: ATLAS9 and ATLAS12 (Castelli & Kurucz 2004), MARCS (Gustafsson et al. 2008) for dwarfs, and LLmodels (Shulyak et al. 2004). All these models assume plane-parallel one-dimensional (1D) geometry and the local thermodynamical equilibrium (LTE). Our calculations were performed with the MARCS models.

3.1 Choice of spectral windows

For stars hotter than 6000 K Torres et al. (2012) found that the SME and SPC (Stellar Parameter Classification, Buchhave et al. 2012) spectrum fitting procedures produce systematically lower effective temperatures and surface gravities compared to the results based on the *EW* measurements and analysis of the Fe I excitation and Fe I/Fe II ionisation equilibria. These authors used spectral intervals similar to those adopted by Valenti & Fischer (2005), which include the 5163–5190 Å spectral region and few small windows in the 6000–6180 Å wavelength range. The first region contains the Mg Ib lines, whose extended wings are sensitive to surface gravity variations in G- and K-type stars, while being less sensitive for F-type stars. Most of the other lines belong to Fe-peak elements. The strong Ca I lines in the 6100–6180 Å spectral range were not included in the fitting.

For the present analysis we have selected four spectral regions to be fitted by SME: 4485–4590 Å, 5100–5200 Å, 5600–5700 Å, and 6100–6200 Å. They include the spectral features, which are sensitive to a variation in different atmospheric parameters. The 4485–4590 Å spectral range includes numerous Ti I–Ti II and Fe I–Fe II lines with accurate laboratory data, making this region very sensitive to gravity variations. The 5100–5200 Å spectral range covers the molecular C₂ (C₂ Swan system) and MgH lines, which are strongly temperature dependent in cool stars. The 5167–5183 Å and 6100–6200 Å intervals include the Mg Ib and strong Ca I lines with Lorentz wings induced by the collisional broadening sensitive to gravity variations.

However, in spectra of stars hotter than the Sun the line broadening due to collisions with hydrogen atoms (i.e., Van der Waals broadening) becomes smaller and the molecular lines disappear. Therefore, the degeneracy between different atmospheric parameters increases, resulting in biases in temperature, gravity, and metallicity. To solve this problem, one needs to use features that are strongly sensitive to one of the parameters, for example the hydrogen Balmer line wings, which are temperature indicators in F-, G-, and K-type stars (Fuhrmann et al. 1993; Cayrel et al. 2011). When dealing with hydrogen lines, the major problem is a correct continuum normalisation, in particular for high-resolution

echelle spectra. We included the H β (4820–4880 Å) and H α (6520–6580 Å) lines in the SME fitting, excluding the ± 1.5 Å regions around the line centers. Also the cores of the strong Mg I and Ca I lines were not considered in the fit because of departures from LTE.

The SME mask was used to remove unidentified features and spectral lines with uncertain atomic parameters. The mask was verified using the solar atlas and then applied to all stars. For individual observations the mask was further corrected to exclude regions showing spectral defects (e.g., dead pixels), remaining cosmics, and telluric lines, particularly in the wings of the H α line. The use of new/extended spectral regions was made possible thanks to a new version of the Vienna Atomic Line Database⁹ (VALD3; Ryabchikova et al. 2015) that includes a new extensive set of atomic line calculations by R. Kurucz¹⁰ and his collection of molecular lines. Also the new data for the C₂ Swan system from Brooke et al. (2013) were included. For lines of Sc, V, Mn, Co, and Cu the full hyperfine structure (HFS) was taken into account (see references on Kurucz’s web site). Hydrogen line profiles were calculated with the code described in Barklem et al. (2000, and references therein)¹¹. For comparison purposes we also run SME using the mask adopted by Valenti & Fischer (2005), including their atomic and molecular line parameters.

We analysed the stars using the four following masks:

- (i) the four regions covering the metal lines (hereafter, m4),
- (ii) m4 plus the H α line (hereafter, m5),
- (iii) m4 plus the H α and H β lines (hereafter, m6), and
- (iv) the mask used by Valenti & Fischer (2005, hereafter, VF)

In total, our masks consist of 331 spectral intervals from six large regions. The masks are available at Table A1 in Appendix. For each star the best fit solution was searched for a set of six free parameters: effective temperature T_{eff} , surface gravity $\log g$, metallicity $[M/H]$, microturbulence velocity V_{mic} , macroturbulence velocity V_{mac} , and projected rotational velocity $V_{\text{rot}} \sin i$. The final T_{eff} , $\log g$, and $[M/H]$ values are listed in Table 1.

3.2 Error analysis

The newly implemented method for estimating uncertainties in the free parameters within SME is based on the fit residuals, partial derivatives, and data uncertainties. We construct a cumulative distribution using all data pixels for a given free parameter p . This distribution describes the fraction of spectral pixels that requires a change of δp or less to achieve a "perfect" fit. Examples of such distributions for different parameters in HD 1461 (UVES spectrum) are given in Figure 1. The position of the data pixels on the x -axis is estimated from the residuals and the partial derivative of the synthetic spectrum over the particular parameter. Probability density distributions for such uncertainty estimate have

⁹ <http://vald.astro.univie.ac.at/vald3/php/vald.php>

¹⁰ <http://kurucz.harvard.edu/atoms.html>

¹¹ <http://www.astro.uu.se/~barklem/hlinop.html>

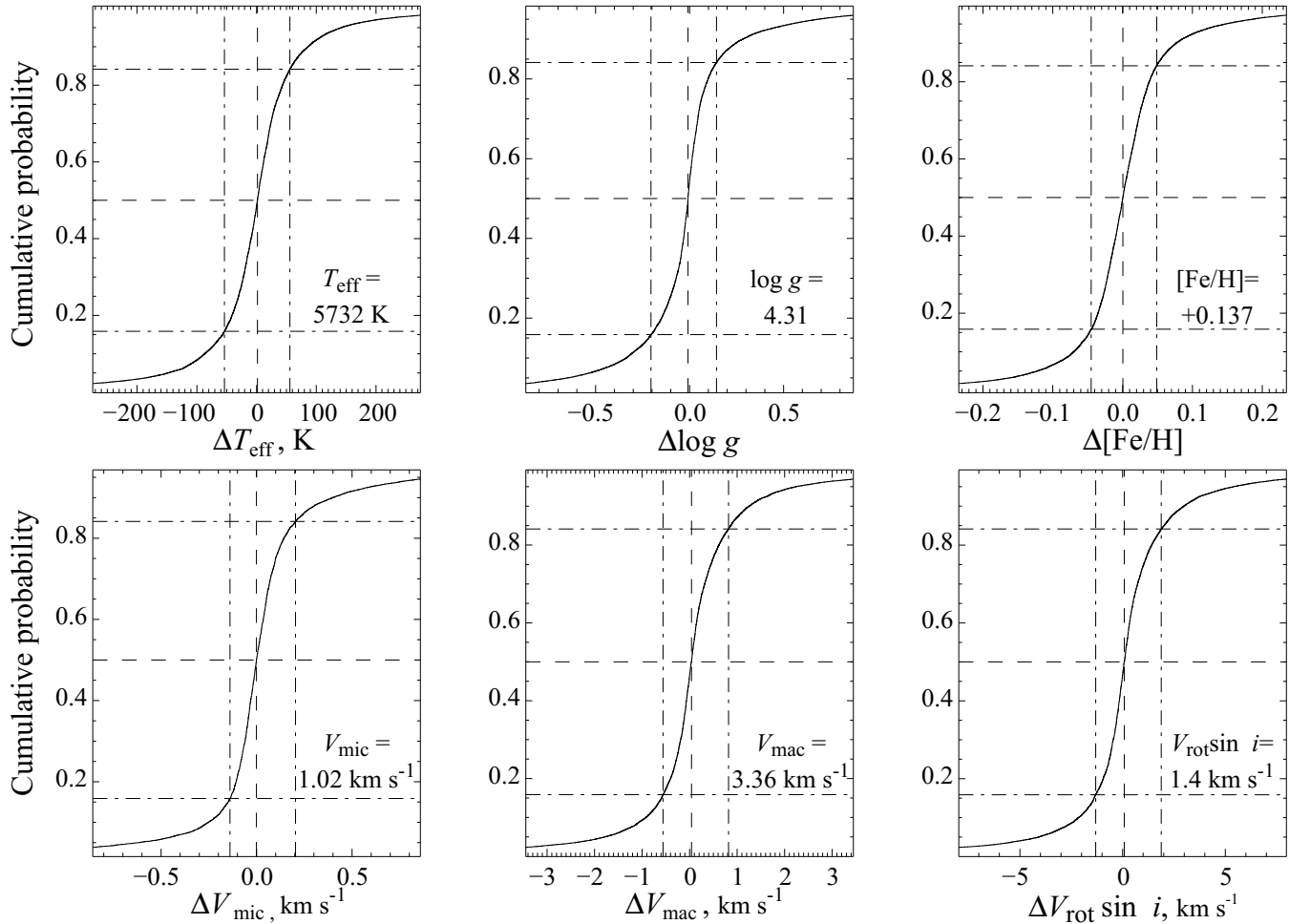


Figure 1. Example of cumulative distributions obtained from SME for T_{eff} , $\log g$, metallicity, microturbulence velocity V_{mic} , macroturbulence velocity V_{mac} , and projected rotational velocity $V_{\text{rot}} \sin i$ for HD 1461 (UVES spectrum). The zero-points of the x-axes are set at the final values obtained with SME. The horizontal dash and dash-dotted lines show the median and the 1σ levels, respectively.

very wide wings due to pixels insensitive to the selected parameter or pixels impossible to fit due to erroneous observations or/and incorrect atomic and molecular data, but they do have a clear central peak. Examples of the central part of the density distributions for the same parameters are given in Figure 2. To guide the reader's eye we also added the best fit Gaussians and marked the median and the $\pm\sigma$ range estimated from the cumulative distributions.

The fact that the central part is not too far from a Gaussian confirms that we can still apply normal distribution standard deviation concept for assessing parameter uncertainties for a bulk of observations; this is anyway more easily done with a cumulative distribution because it does not require an a priori knowledge of the bin size and of the clipping range for the central part. The final parameter uncertainty includes both systematic uncertainty (model limitations) and the observational one. While our method still ignores the cross-talk between different parameters it shows massive improvement over the uncertainties based on the covariance matrix (also evaluated by SME). The uncertainties derived from the diagonal of the covariance matrix are effectively a projection of the observational errors onto the model parameter space using partial derivatives averaged

over all data pixels. For high S/N observations the contribution of the observational errors is negligible in comparison to model limitations, and the resulting uncertainty estimates are unrealistically small. The mathematical background of the new approach can be found in the upcoming paper by Piskunov & Valenti (2015).

Note that the estimated median values in Fig. 1 are close to, but not exactly matching, the SME result. The reason is that the error estimate procedure presented here is not taking into account the degeneracy/correlation between parameters. The final estimated errors are listed in Table 1. The starting points used for the SME's optimisation algorithm were taken close to the previously published parameters. We check the robustness of the convergence algorithm implemented in SME by performing 1000 runs for the ESPaDONS spectrum of HD 69830 (mask4) with initial guesses for T_{eff} , $\log g$, and $[M/H]$ equally spaced across the volume: [4972:5872; 4.015:4.915; -0.4945:0.4055]. The solutions were found to converge within 3 K in T_{eff} , 0.005 dex in $\log g$, and 0.002 dex in $[M/H]$.

The influence of the continuum rectification on the final atmospheric parameters was checked in the following way. For three stars of different effective temperature and grav-

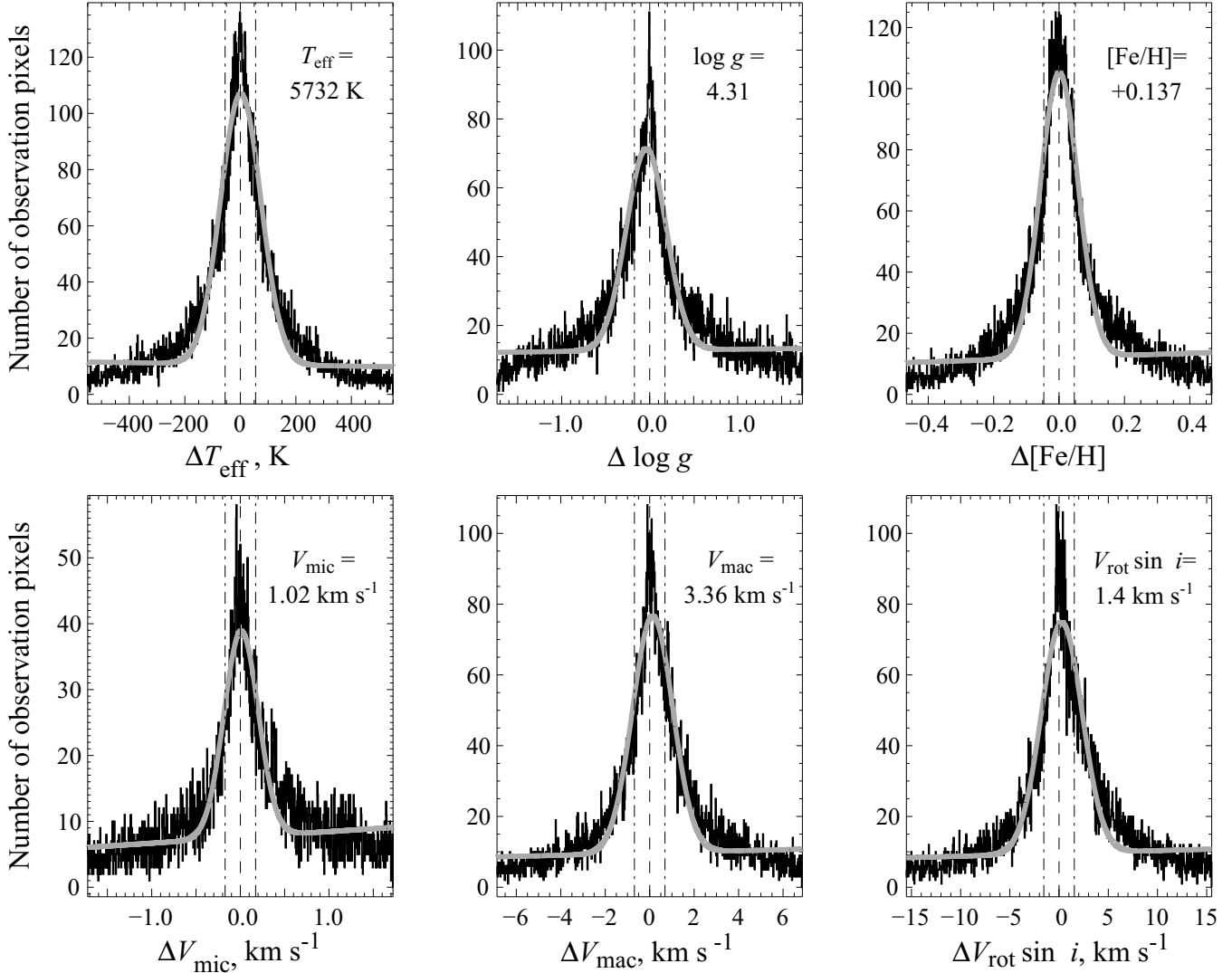


Figure 2. Example of density distributions for the same parameters as in Figure 1. Best fit Gaussians of the central peaks are shown by gray colour. Dashed and dash-dotted lines indicate the median and the $\pm\sigma$ range estimated from the cumulative distributions.

ity, HD 9826, HD 69830, and HD 23249, we run SME with the m4 and m6 masks using observations with the continuum rectification independently made by three of us, i.e. T. Ryabchikova, Yu. Pakhomov, and L. Fossati; we did not find any systematic bias in our parameter determinations caused by the different continuum placements. The differences in the derived gravity and metallicity did not exceed 0.03 dex and 0.01 dex, respectively. For the effective temperature, a maximum difference of 20 K was obtained for HD 69830, but this value is smaller than the uncertainty.

A close look at the results presented in Table 1 shows that the spectral resolution of the observations does not significantly affect the derived parameters: the overall difference in the effective temperature, surface gravity, and metallicity does not exceed the error bars. Figure 3 shows that the uncertainties in temperature and gravity increase with increasing effective temperature. In order to consistently compare the uncertainties for each star, all error bars have been interpolated in order to provide the uncertainties obtained from a spectrum with $S/N = 200$. Figure 3 shows that a rel-

ative uncertainty in the effective temperature changes from 1 % to 2 % over the 5000–6700 K temperature range.

We further checked a dependence of the derived parameters and their uncertainties on the spectrum quality (i.e., S/N). We took the ESPaDONs spectrum of HD 69830 and introduced an additional white noise component in order to decrease the S/N . In the SME analysis we used the common initial parameters for each spectrum. The results are shown in Fig. 4. The T_{eff} values derived from different spectra agree within ± 20 K, while the $\log g$ values range between 4.38 and 4.53, not centering at $\log g = 4.49$ that was derived from the spectrum with the highest S/N . A similar behaviour was also found for the metallicity. For the effective temperature, surface gravity, and metallicity SME finds solutions in a range much smaller than the typical error estimates. Our conclusion is therefore that the S/N should not have a great influence on the derived parameters even though the error bars increase dramatically with decreasing S/N .

For high S/N spectra the derived uncertainty is driven by model limitations (systematic error). In our case these

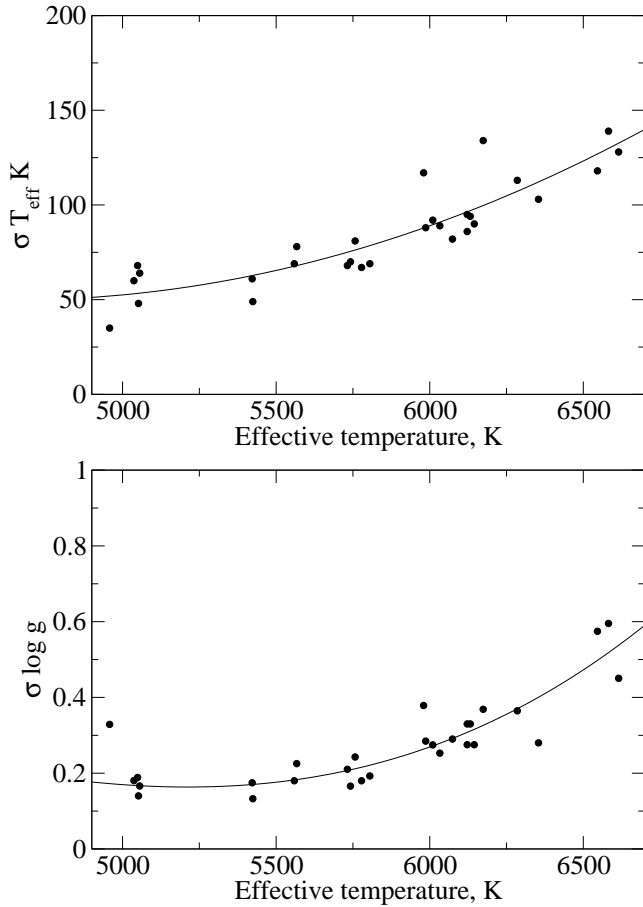


Figure 3. Uncertainty in the effective temperature (top) and surface gravity (bottom) as a function of the effective temperature. The solid line shows the quadratic polynomial fit to the data.

systematic errors are ± 20 – 30 K in T_{eff} , ± 0.05 – 0.08 dex in $\log g$, and ± 0.02 dex in $[\text{M}/\text{H}]$, if we consider spectra with $\text{S/N} \geq 1000$. We also checked the possible effect of the model grids used in SME on the derived parameters. For a few, including the Sun, we run SME with ATLAS9 and LLmodels grids of stellar atmospheres. LLmodels give effective temperatures of 10–15 K higher than MARCS models for stars cooler than the Sun and of 10–20 K lower for hotter stars. Surface gravity changes by less than $+0.02$ dex for stars with $T_{\text{eff}} > 5700$ K and by $+0.03$ – $+0.05$ dex for cooler stars. Metallicity is practically unaffected. With ATLAS9 models the corresponding changes are -30 K to $+50$ K in T_{eff} and -0.03 dex or less in surface gravity. All these changes lie within the error limits obtained with MARCS models. The comparison for the solar spectrum allows us to evaluate possible offsets, because the Sun is then only star with a direct, model independent determination of the effective temperature and surface gravity. We obtain possible offsets of -20 K, -0.03 dex, -0.03 dex for effective temperature, surface gravity and metallicity. All these values are compatible with the corresponding errors given by spectrum fitting.

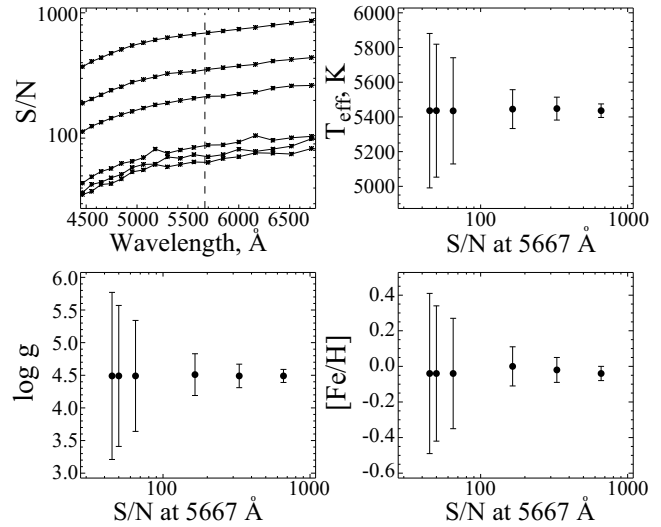


Figure 4. Dependence of the inferred atmospheric parameters (T_{eff} , $\log g$, and $[\text{M}/\text{H}]$) and their uncertainties on the S/N of the observed spectra. The top-left panel gives the S/N in logarithmic scale as a function of wavelength.

4 ANALYSIS OF THE DERIVED ATMOSPHERIC PARAMETERS

We compare here the obtained atmospheric parameters with those present in the literature and based on interferometric and spectroscopic methods.

4.1 Comparison with the interferometric parameters

From interferometric data, the effective temperature is derived from the measured angular diameter and bolometric flux. The interferometric T_{eff} for Procyon, HD 49933, ν And, β Vir, δ Eri, and HD 103095 were extracted from Boyajian et al. (2013, and references therein). For other stars the corresponding data were taken from Boyajian et al. (2015, HD 209458 and HD 189733), von Braun et al. (2014, HD 1461 and 61 Vir), and Tanner et al. (2015, HD 69830). These values are listed in Table 1. Bolometric fluxes for all stars were calculated using the spectral energy distribution (SED) fitting code presented by van Belle et al. (2008). For the solar atmosphere we used the canonical parameters (Christensen-Dalsgaard et al. 1996). Three stars have two or more independent measurements of the angular diameter (see Boyajian et al. 2013, and references therein).

For Procyon the angular diameter measurements lead to effective temperatures that agree within the quoted uncertainties. For the other two stars, with quoted uncertainties of ~ 25 K or less, the interferometric temperatures differ by 60 K to 150 K. While the effective temperature is a measured parameter, though indirect, the surface gravity is only inferred from the stellar radius measured with interferometry and the star’s mass, derived on the basis of evolutionary tracks. There are two stars, HD 209458 and HD 189733, for which the surface gravities have been derived from the binary solution obtained from the analysis of the transit and radial velocity curves of their planets (Boyajian et al. 2015). We estimated the uncertainty in $\log g$ assuming a 5 % un-

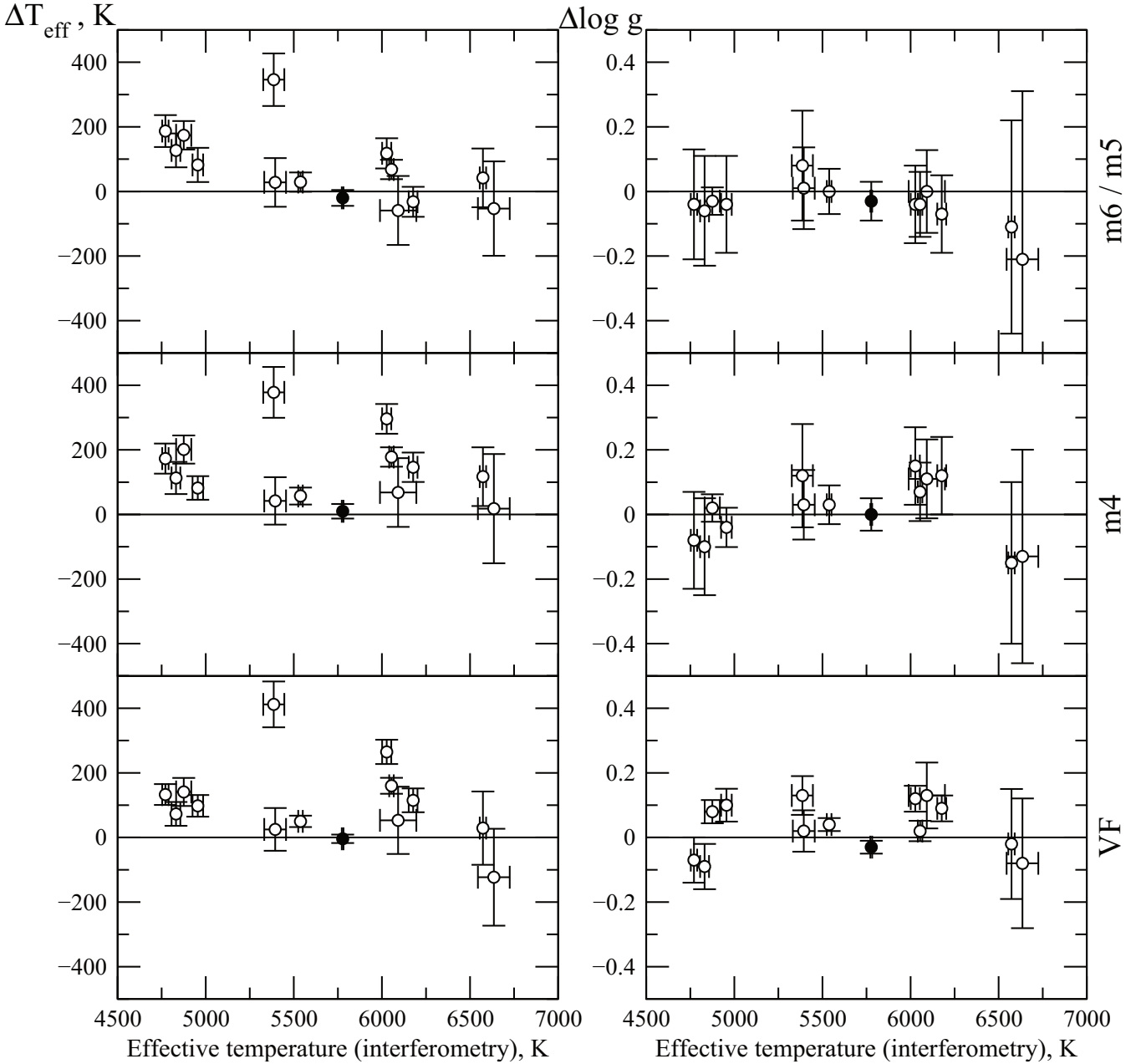


Figure 5. Differences between the SME and interferometric T_{eff} (left) and $\log g$ (right) values as a function of the interferometric effective temperature. The differences are shown on the basis of the adopted masks for the SME analysis: m6/m5 (top), m4 (middle), and VF (bottom). The Sun is shown by a filled circle.

certainty in the mass given by Boyajian et al. (2013) and the quoted uncertainty in the measured radius.

Figure 5 shows the differences between the SME (using different masks) and interferometric T_{eff} and $\log g$ values as a function of the interferometric effective temperature. For stars hotter than the Sun the closest agreement with the interferometric parameters is achieved, when using the m6 or m5 masks within SME, while the other two masks tend to overestimate the effective temperature. Below 5000 K we obtain systematically higher effective temperatures compared to those derived from interferometry, however, our results agree well with those obtained with other spectroscopic methods (see Sect. 4.2). The only outlier is

HD 1461: we believe that its measured angular diameter is too high resulting in lower effective temperature. Plenty of different modern methods of parameter determination provide results for HD 1461 which agree with each other, but not with the interferometric ones (see the PASTEL catalogue of stellar parameters; Soubiran et al. 2010). When excluding this particular star, the average temperature differences between the SME and interferometric values are 50 K, 80 K, and 120 K for m6, VF, and m4 masks, respectively. When considering instead only stars hotter than 5100 K, the corresponding average differences are 18 K, 60 K, and 110 K. In all comparisons the standard deviation in T_{eff} varies from 60 K (m6) to 90 K (m4, VF). The difference in $\log g$ varies

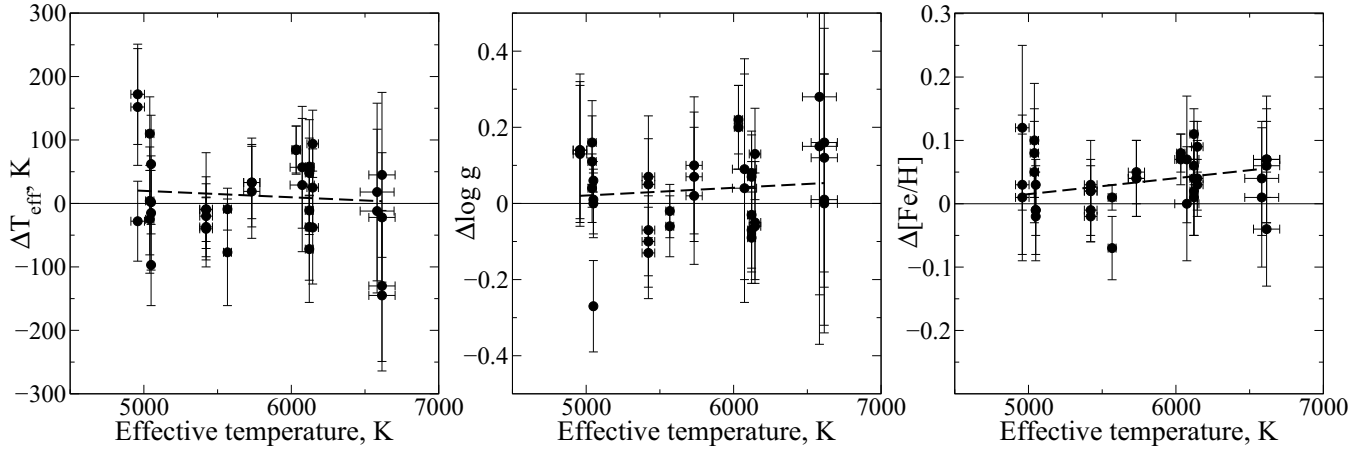


Figure 6. Differences in temperature (left), gravity (center), and metallicity (right) between the SME analysis with the m6/5 masks and the corresponding literature spectroscopic values as a function of the SME effective temperature. Linear regressions weighted by the uncertainties are indicated by dashed lines.

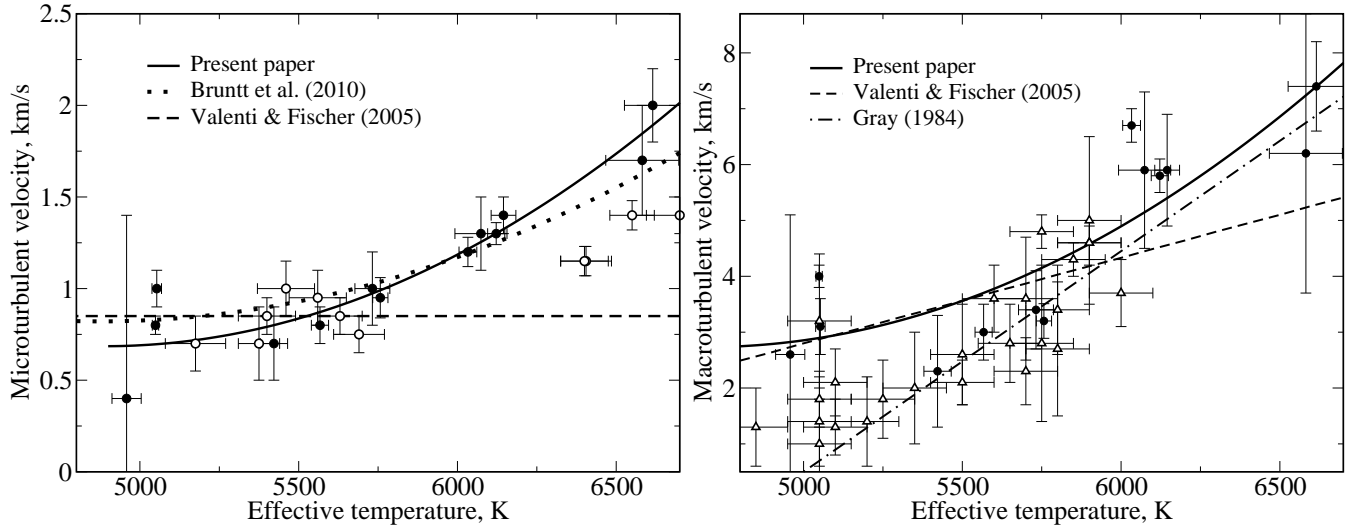


Figure 7. Dependence of V_{mic} (left panel) and V_{mac} (right panel) on the effective temperature. The results of the present paper are shown by filled circles. The quadratic polynomial fits of our results are shown by solid lines in both panels. Open circles show the V_{mic} values from Doyle et al. (2013), while open triangles show the V_{mac} data from Saar & Osten (1997). The sources for analytical approximations are quoted in each panel

from -0.04 dex (m6) to $+0.04$ dex (m4, VF) with a standard deviation of 0.08 dex.

4.2 Comparison with other spectroscopic studies

Table 1 lists the atmospheric parameters derived in the literature using various spectroscopic methods, together with their sources, and Fig. 6 displays the differences in temperature, gravity, and metallicity between the SME analysis with the m6/m5 masks and the corresponding literature data. No significant trends and offsets are found. Using the VF and m4 masks leads to an overestimation of all three parameters for the hottest stars. Instead, using the mask including the hydrogen lines (m6/m5) removes this offset.

The average difference between the stellar parameters derived with SME (m6/m5 masks) and other spectro-

scopic methods was found to be 12 ± 66 K for the effective temperature, 0.04 ± 0.12 dex for the surface gravity, and 0.04 ± 0.04 dex for the metallicity. It may be considered as method-to-method dispersion. The dispersion values corresponds to the error estimates derived by SME for $S/N=200$.

4.3 Micro- and macroturbulent velocities

When deriving atmospheric parameters for a large number of stars by means of a spectrum fitting technique, both micro and macroturbulent velocities (V_{mic} and V_{mac}) are usually not directly estimated, but are either fixed (e.g., V_{mic} in Valenti & Fischer 2005) or estimated on the basis of analytical approximations (e.g., V_{mac} in Torres et al. 2012). Our SME analysis allowed us to derive both these parameters, with the corresponding error bars, for each star. Figure 7

shows stellar V_{mic} and V_{mac} parameters as a function of the effective temperature.

In general, our measurements agree with those given by previous studies. The analytical expression by Bruntt et al. (2010) for V_{mic} seems to fit our data in a reasonable way, while using a fixed value of V_{mic} would be inappropriate for stars hotter than 6000 K. The analytical formula proposed by Valenti & Fischer (2005) underestimates V_{mac} for the hottest stars, while it reasonably represents our measurements for stars cooler than 5500 K. The Gray (1984) formula seems to be a good approximation for V_{mac} in stars hotter than the Sun.

5 ABUNDANCES

We test the atmospheric parameters obtained with the m6 mask by inspecting abundances from two ionisation stages for Ti and Fe and from the atomic C I and molecular CH species. The elements Ti and Fe were chosen because of the large number of lines with precise laboratory atomic data available at optical wavelengths. For Ti I and Ti II we used the homogeneous set of laboratory transition probabilities by Lawler et al. (2013) and Wood et al. (2013), while for Fe I and Fe II the line parameters were extracted from the third version of the VALD database (Ryabchikova et al. 2015). We also considered the C abundance derived from atomic C I and molecular CH lines that are known to be sensitive to T_{eff} variations. Line parameters were also extracted from VALD. While the C₂ Swan system lines were included in fitting procedure, for abundances we employed the CH lines in 4200-4400 Å region because these lines are strong and are easily measured in spectra of all stars of our program. Unblended C₂ lines suitable for abundance determinations practically disappeared in spectra of stars hotter than 6000 K. A list of the lines used for the abundance determination, together with the adopted line parameters, is given in Table 2 (online material). In total we used 8 lines of C I in the visible and near IR regions, 8 bands of CH, 21 lines of Ti I, 10 lines of Ti II, 73 lines of Fe I, and 28 lines of Fe II.

Element abundances from the atomic lines were calculated based on the non-local thermodynamic equilibrium (NLTE) line formation. To solve the coupled radiative transfer and statistical equilibrium (SE) equations, we used a revised version of the DETAIL code (Butler & Giddings 1985). The update was described by Mashonkina et al. (2011). In the atmospheric parameter range covered by the analysed stars, departures from LTE are negligible for Ti II and Fe II lines and small for lines of Ti I and Fe I and lines of C I in the visible spectral range. The molecular CH lines are considered to be free of NLTE effects. For Ti I and Ti II the NLTE calculations were performed using a comprehensive model atom constructed by Sitnova et al. (2015). For cool stars the main source of uncertainty in NLTE calculations for Ti I (as well as for Fe I) is poorly known inelastic collision with hydrogen atoms. In this study they are treated employing the Drawinian (Drawin 1968, 1969) rates scaled by a factor of $S_H = 0.5$. It is worth noting that for HD 49933 ($T_{\text{eff}} = 6580$ K; $\log g = 4.0$; $[M/H] = -0.48$ dex) using $S_H = 0.5$ leads to 0.019 dex higher average abundance from the Ti I lines compared to that for $S_H = 1.0$.

Table 2. Atomic and molecular line parameters

Wavelength, Å	Ion	E_i , eV	$\log(gf)$	Reference
4218.7130	CH	0.411	-1.339	1
4218.7340	CH	0.411	-1.361	1
...
4489.7391	Fe I	0.121	-3.966	2
4491.3971	Fe II	2.856	-2.700	3
4493.5220	Ti II	1.080	-2.780	4
...

References: (1) Jorgensen et al. (1996); (2) Fuhr et al. (1988); (3) Kroll & Kock (1987); (4) Wood et al. (2013); (5) Raassen & Uylings (1998); (6) Lawler et al. (2013); (7) Ryabchikova et al. (1999); (8) Baschek et al. (1970); (9) Kurucz (2015); (10) O'Brian et al. (1991); (11) Ralchenko et al. (2010); (12) Blackwell et al. (1980) (corrected); (13) Bard et al. (1991); (14) Hannaford et al. (1992); (15) Bard & Kock (1994); (16) May et al. (1974); (17) Allende Prieto et al. (2002).

(This table is available in its entirety in a machine-readable form in the online journal. A portion is shown here for guidance regarding its form and content.)

Effect of varying S_H is even smaller for the Sun, with a difference of 0.008 dex between applying $S_H = 0.5$ and 1.0. For iron, we used a comprehensive Fe I-Fe II model atom treated by Mashonkina et al. (2011) and employed $S_H = 0.5$, as deduced by (Sitnova et al. 2015) from analysis of the nearby dwarf stellar sample. The NLTE calculations for the C I lines were performed with the method from Alexeeva & Mashonkina (2015).

The departure coefficients (the ratios of NLTE to LTE level populations) calculated for each atmospheric model with the DETAIL code were then implemented in the SYNTHV_NLTE code. This software, presented in Tsymbal (1996), calculates the spectrum emerging from the static, 1-D model atmosphere, and it was tuned for the modelling of early B- to late M-type stars. The code was originally employing the LTE approximation, and in this study it was modified to take into account the pre-computed departure coefficients for various chemical species. We further integrated it within the IDL BINMAG3 code¹², written by O. Kochukhov, finally allowing us to determine the best fit to the observed line profiles with the inclusion of the NLTE effects. The spectrum synthesis code adopted by SME and the SYNTHV_NLTE code use different algorithms for the radiative transfer solution, which may result in systematic differences in the derived abundances. We compared the two codes as follows. We used the synthetic spectrum computed by SME for HD 69830 (ESPADONS spectrum) in the 5640-50 Å wavelength region as the “observed spectrum” for (SYNTHV_NLTE + BINMAG3). In the latter code, abundances of eight elements listed in Table 3 were allowed to vary, when fitting the SME ‘observed spectrum’. Table 3 shows the LTE abundances from calculations with SME and SYNTHV_NLTE + BINMAG3. The SME code returns an overall element abundance based on all the lines of each given element in the SME spectral windows, while SYNTHV_NLTE + BINMAG3 provides abundances from individ-

¹² <http://www.astro.uu.se/~oleg/download.html>

Table 3. LTE abundances derived by SME for HD 69830 (second column) and by SYNTHV_NLTE + BINMAG3 for the SME 'observed spectrum' (third column). See text for more details.

Element	Abundance $\log(N_{el}/N_{tot})$	
	SME	synthV_NLTE+ binmag (LTE)
Si	-4.57(0.17)	-4.56
Sc	-8.87(0.04)	-8.87
Ti	-7.11(0.07)	-7.11
V	-8.11(0.06)	-8.10
Cr	-6.44(0.07)	-6.42
Fe	-4.60(0.06)	-4.59
Co	-7.23(0.10)	-7.22
Ni	-5.87(0.05)	-5.86

ual lines, which were averaged for each given element. It can be seen that the two different spectrum synthesis codes used in our study provide consistent abundances within 0.02 dex.

Stellar abundances of C, Ti, and Fe calculated with the adopted atmospheric models using SYNTHV_NLTE + BINMAG3 are presented in Table 4. The abundance differences between the two ionisation stages for Ti and Fe and between the atomic C I and molecular CH species are shown in Fig. 8. We consider ± 0.05 dex to be the typical error bars for our abundance determination. Such an uncertainty corresponds to that obtained by a variation of ± 0.1 dex in the surface gravity and ± 50 –70 K in the effective temperature for solar-type stars. This agrees with the results presented in Sect. 4.1 and 4.2. For all the stars, except HD 189733 and HD 23249, the ionisation equilibria are achieved within 0.05 dex.

For HD 189733 and HD 23249 their carbon abundances derived from the atomic and molecular lines are consistent, while the Ti I–Ti II and Fe I–Fe II abundance differences reach +0.10 dex. These positive differences may indicate an overestimation of the effective temperature as derived by SME and support the lower effective temperature from interferometry. We inspected abundances of C, Ti, and Fe calculated with the interferometric atmospheric parameters, and we obtained an abundance difference of ~ -0.10 dex for Ti I–Ti II and Fe I–Fe II and a very large difference of 0.4 dex between C I and CH. Most likely, for both stars their effective temperatures lie in between the SME and the interferometric values.

6 CONCLUSIONS

We used a sample of well studied F-, G-, and K-type stars to perform an extensive test of the accuracy of atmospheric parameters derived with the fitting procedure SME, widely applied in the literature for late-type stars. In our analysis we used high-quality and high-resolution spectra obtained with a wide range of different instruments and telescopes. We adopted three different masks for the spectral analysis and implemented a new, more accurate scheme for the determination of the uncertainties in the atmospheric parameters. We would like to emphasise that our approach provides self-consistent spectroscopic results without any external constraints on any of five atmospheric parameters: T_{eff} , $\log g$, $[M/H]$, V_{mic} , and V_{mac} .

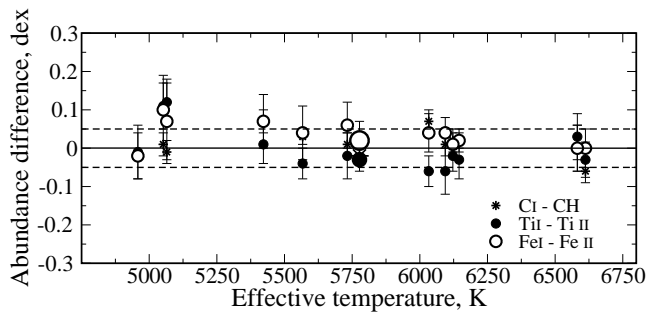


Figure 8. Abundance differences between the atomic C I and molecular CH lines (stars), between lines of Ti I and Ti II (filled circles), and between lines of Fe I and Fe II (open circles). The solar values are shown by larger size symbols. The solid line shows the perfect ionisation balance, while the dashed lines indicate the $\sigma = \pm 0.05$ dex level.

We compared our results with those obtained with interferometry arriving at the following conclusions.

- Atmospheric parameters derived with SME on the basis of different masks agree within the uncertainties for stars cooler than 5500 K, while for hotter stars we recommend to include the H β and/or H α lines to the spectrum fitting procedure.
- The uncertainty in the effective temperature is 50–70 K for the S/N = 200 spectra of the main-sequence F-, G-, K-type stars.
- Given the spectral ranges, spectral resolution, and S/N values explored here, we were unable to measure surface gravity with an accuracy of $\log g$ better than 0.1 dex using SME.
- The typical uncertainty in the metallicity derived with SME is 0.05–0.06 dex.

ACKNOWLEDGEMENTS

This work was supported by the Federal Agency for Science and Innovations (grant No. 8529), the Russian Foundation for Basic Research (grant 15-02-06046). T.S. and S.A. thank the RFBR grant 14-02-31780. L.M. and T.S. are thankful to the Swiss National Science Foundation (SCOPES project No. IZ73Z0-152485) for partial financial support. This study is based on observations made with ESO Telescopes at the La Silla Paranal Observatory under programme ID 085.D-0124 and MegaPrime/MegaCam, a joint project of CFHT and CEA/IRFU, at the CFHT, which is operated by the National Research Council (NRC) of Canada, the Institut National des Science de l'Univers of the Centre National de la Recherche Scientifique (CNRS) of France, and the University of Hawaii. We employed the data products produced at Terapix available at the Canadian Astronomy Data Centre as part of the Canada-France-Hawaii Telescope Legacy Survey, a collaborative project of NRC and CNRS. This research has made use of the Keck Observatory Archive (KOA), which is operated by the W. M. Keck Observatory and the NASA Exoplanet Science Institute (NExSci), under contract with the National Aeronautics and Space Administration. The Observatory was made possible by the generous

Table 4. NLTE abundances of C, Ti, and Fe derived from the atomic lines and the LTE abundances from the molecular CH lines together with their standard deviations given in parentheses.

Name/HD	T_{eff} , K	$\lg g$	Abundance $\log(N_{\text{el}}/N_{\text{tot}})$					
			CH	C I	Ti I	Ti II	Fe I	Fe II
Sun	5777	4.44	−3.60(02)	−3.62(01)	−7.09(03)	−7.06(04)	−4.55(05)	−4.57(06)
Procyon	6615	3.89	−3.59(02)	−3.66(01)	−7.12(06)	−7.09(08)	−4.57(05)	−4.57(08)
HD 49933	6582	4.00	−4.09(05)	−4.09(02)	−7.52(06)	−7.55(04)	−5.08(06)	−5.08(06)
HD 9826	6145	4.06	−3.62(01)	−3.59(02)	−7.04(05)	−7.01(06)	−4.48(07)	−4.50(06)
HD 102870	6122	4.07	−3.53(03)	−3.51(03)	−6.96(04)	−6.94(05)	−4.40(06)	−4.41(06)
HD 149026	6074	4.18	−3.42(03)	−3.41(02)	−6.87(06)	−6.81(06)	−4.27(06)	−4.31(06)
HD 209458	6033	4.28	−3.78(02)	−3.71(02)	−7.14(04)	−7.08(05)	−4.58(06)	−4.62(05)
HD 1461	5732	4.31	−3.50(02)	−3.49(02)	−6.95(06)	−6.94(06)	−4.38(06)	−4.43(05)
HD 115617	5567	4.42	−3.72(02)	−3.71(03)	−7.09(04)	−7.05(06)	−4.58(07)	−4.62(06)
HD 69830	5422	4.47	−3.72(02)	−3.66(05)	−7.07(05)	−7.08(06)	−4.57(07)	−4.63(06)
HD 189733	5065	4.55	−3.74(03)	−3.75(04)	−6.98(06)	−7.10(06)	−4.53(10)	−4.60(09)
HD 23249	5052	3.76	−3.61(03)	−3.60(03)	−6.89(07)	−7.00(06)	−4.45(09)	−4.55(07)
HD 103095	4958	4.52	−5.17(05)		−8.23(08)	−8.22(06)	−5.94(06)	−5.92(05)

financial support of the W.M. Keck Foundation. We thank anonymous referee for the insightful remarks.

REFERENCES

- Alexeeva S. A., Mashonkina L. I., 2015, *MNRAS*, 453, 1619
Allende Prieto C., Lambert D. L., Asplund M., 2002, *ApJ*, 573, L137
Bagnulo S., Jehin E., Ledoux C., Cabanac R., Melo C., Gilmozzi R., ESO Paranal Science Operations Team 2003, *The Messenger*, 114, 10
Bard A., Kock A., Kock M., 1991, *A&A*, 248, 315
Bard A., Kock M., 1994, *A&A*, 282, 1014
Barklem P. S., Piskunov N., O'Mara B. J., 2000, *A&A*, 363, 1091
Baschek B., Garz T., Holweger H., Richter J., 1970, *A&A*, 4, 229
Blackwell D. E., Shallis M. J., Simmons G. J., 1980, *Astron. and Astrophys.*, 81, 340
Blanco-Cuaresma S., Soubiran C., Jofré P., Heiter U., 2014, *A&A*, 566, A98
Boyajian T., von Braun K., Feiden G. A., Huber D., Basu S., et al., 2015, *MNRAS*, 447, 846
Boyajian T. S., von Braun K., van Belle G., Farrington C., Schaefer G., et al., 2013, *ApJ*, 771, 40
Brooke J. S. A., Bernath P. F., Schmidt T. W., Bacskay G. B., 2013, *J. Quant. Spec. Radiat. Transf.*, 124, 11
Bruntt H., 2009, *A&A*, 506, 235
Bruntt H., Bedding T. R., Quirion P.-O., Lo Curto G., Carrier F., et al., 2010, *MNRAS*, 405, 1907
Buchhave L. A., Latham D. W., Johansen A., Bizzarro M., Torres G., et al., 2012, *Nature*, 486, 375
Butler K., Giddings J., 1985, *Newsletter on the analysis of astronomical spectra*, No. 9, University of London
Castelli F., Kurucz R. L., 2004, in Piskunov N., Weiss W., Gray D., eds, *Modelling of Stellar Atmospheres Proceedings of the IAU Symp. No 210, New Grids of ATLAS9 Model Atmospheres*
Cayrel R., van't Veer-Menneret C., Allard N. F., Stehlé C., 2011, *A&A*, 531, A83
Christensen-Dalsgaard J., Dappen W., Ajukov S. V., Anderson E. R., Antia H. M., et al., 1996, *Science*, 272, 1286
de la Cruz Rodríguez J., Piskunov N., 2013, *ApJ*, 764, 33
Doyle A. P., Smalley B., Maxted P. F. L., Anderson D. R., Cameron A. C., et al., 2013, *MNRAS*, 428, 3164
Drawin H.-W., 1968, *Zeitschrift für Physik*, 211, 404
Drawin H. W., 1969, *Zeitschrift für Physik*, 225, 483
Fuhr J. R., Martin G. A., Wiese W. L., 1988, *Journal of Physical and Chemical Reference Data*, Volume 17, Suppl. 4. New York: American Institute of Physics (AIP) and American Chemical Society, 1988, 17
Fuhrmann K., 1998, *A&A*, 338, 161
Fuhrmann K., 2008, *MNRAS*, 384, 173
Fuhrmann K., Axer M., Gehren T., 1993, *A&A*, 271, 451
Gilmore G., Randich S., Asplund M., Binney J., Bonifacio P., Drew J., Feltzing S., Ferguson A., Jeffries R., Micela G., et al. 2012, *The Messenger*, 147, 25
Gonzalez G., Carlson M. K., Tobin R. W., 2010, *MNRAS*, 403, 1368
Gray D. F., 1984, *ApJ*, 281, 719
Gustafsson B., Edvardsson B., Eriksson K., Jørgensen U. G., Nordlund Å., et al., 2008, *A&A*, 486, 951
Hannaford P., Lowe R. M., Grevesse N., Noels A., 1992, *A&A*, 259, 301
Heiter U., Jofré P., Gustafsson B., Korn A. J., Soubiran C., Thévenin F., 2015, *ArXiv Astrophysics e-prints*, astro-ph/1506.06095
Howard A. W., Johnson J. A., Marcy G. W., Fischer D. A., Wright J. T., et al., 2010, *ApJ*, 721, 1467

Jorgensen U. G., Larsson M., Iwamae A., Yu B., 1996, *A&A*, 315, 204

Kroll S., Kock M., 1987, *Astron. and Astrophys. Suppl. Ser.*, 67, 225

Kurucz R. L., , 2015, On-line database of observed and predicted atomic transitions, <http://kurucz.harvard.edu/atoms>

Kurucz R. L., Furenlid I., Brault J., Testerman L., 1984, *Solar flux atlas from 296 to 1300 nm*. New Mexico: National Solar Observatory

Lawler J. E., Guzman A., Wood M. P., Sneden C., Cowan J. J., 2013, *ApJS*, 205, 11

Mashonkina L., Gehren T., Shi J.-R., Korn A. J., Grupp F., 2011, *A&A*, 528, A87

May M., Richter J., Wichelmann J., 1974, *A&AS*, 18, 405

O'Brian T. R., Wickliffe M. E., Lawler J. E., Whaling W., Brault J. W., 1991, *Journal of the Optical Society of America B Optical Physics*, 8, 1185

Piskunov N., Valenti J. A., 2015, *ApJ*, in preparation

Raassen A. J. J., Uylings P. H. M., 1998, *A&A*, 340, 300

Ralchenko Y., Kramida A., Reader J., NIST ASD Team, 2010, *NIST Atomic Spectra Database (ver. 4.0.0)*, <http://www.nist.gov/pml/data/asd.cfm>

Ramírez I., Meléndez J., Asplund M., 2009, *A&A*, 508, L17

Ryabchikova T., Piskunov N., Kurucz R. L., Stempels H. C., Heiter U., et al., 2015, *Phys. Scr*, 90, 054005

Ryabchikova T. A., Piskunov N. E., Stempels H. C., Kupka F., Weiss W. W., 1999, *Phys. Scr* Volume T, 83, 162

Saar S. H., Osten R. A., 1997, *MNRAS*, 284, 803

Santos N. C., Israelian G., Mayor M., 2004, *A&A*, 415, 1153

Shulyak D., Tsymbal V., Ryabchikova T., Stütz C., Weiss W. W., 2004, *A&A*, 428, 993

Sitnova T., Mashonkina L., Ryabchikova T., 2015, in preparation

Sitnova T., Zhao G., Mashonkina L., Chen Y., Liu F., Pakhomov Y., Tan K., Bolte M., Alexeeva S., Grupp F., Shi J.-R., Zhang H.-W., 2015, *ApJ*, 808, 148

Smiljanic R., Korn A. J., Bergemann M., Frasca A., Magrini L., et al., 2014, *A&A*, 570, A122

Soubiran C., Le Campion J.-F., Cayrel de Strobel G., Caillo A., 2010, *A&A*, 515, A111

Sousa S. G., Santos N. C., Israelian G., Mayor M., Monteiro M. J. P. F. G., 2006, *A&A*, 458, 873

Sousa S. G., Santos N. C., Mayor M., Udry S., Casagrande L., et al., 2008, *A&A*, 487, 373

Tanner A., Boyajian T. S., von Braun K., Kane S., Brewer J. M., et al., 2015, *ApJ*, 800, 115

Torres G., Fischer D. A., Sozzetti A., Buchhave L. A., Winn J. N., et al., 2012, *ApJ*, 757, 161

Torres G., Winn J. N., Holman M. J., 2008, *ApJ*, 677, 1324

Tsymbal V., 1996, in Adelman S. J., Kupka F., Weiss W. W., eds, *M.A.S.S., Model Atmospheres and Spectrum Synthesis Vol. 108 of Astronomical Society of the Pacific Conference Series, STARSF: A Software System For the Analysis of the Spectra of Normal Stars*. p. 198

Valenti J. A., Fischer D. A., 2005, *ApJS*, 159, 141

Valenti J. A., Piskunov N., 1996, *A&AS*, 118, 595

van Belle G. T., van Belle G., Creech-Eakman M. J., Coyne J., Boden A. F., et al., 2008, *ApJS*, 176, 276

von Braun K., Boyajian T. S., van Belle G. T., Kane S. R., Jones J., et al., 2014, *MNRAS*, 438, 2413

Wood M. P., Lawler J. E., Sneden C., Cowan J. J., 2013,

ApJS, 208, 27

APPENDIX A:

This paper has been typeset from a \LaTeX file prepared by the author.

Table A1. Laboratory wavelengths of the mask m6. The beginning of each region marked by bold face.

First and last wavelengths, Å					
4485.468–4486.101	4551.114–4551.445	4865.521–4866.407	5193.964–5199.393	6110.657–6111.972	6524.252–6525.690
4487.957–4490.926	4551.560–4551.914	4867.344–4869.003	5597.997–5598.714	6112.400–6113.743	6526.200–6526.773
4491.260–4491.449	4553.698–4553.938	4869.354–4869.523	5599.274–5600.566	6113.933–6115.053	6526.966–6527.376
4491.560–4491.961	4554.133–4556.343	4869.800–4870.212	5602.151–5602.412	6116.792–6117.098	6527.740–6527.972
4492.173–4493.621	4556.652–4557.053	4870.687–4871.518	5602.644–5603.527	6117.968–6120.606	6528.219–6528.366
4494.423–4494.813	4557.970–4558.887	4871.863–4875.116	5603.968–5607.261	6120.898–6122.144	6528.807–6529.318
4495.337–4495.660	4559.851–4560.367	4875.371–4876.600	5607.494–5608.483	6122.293–6123.008	6529.512–6529.876
4495.861–4496.341	4560.619–4562.433	4877.489–4877.654	5608.797–5609.562	6123.927–6126.413	6530.147–6530.433
4496.731–4497.791	4562.548–4562.789	4877.948–4879.939	5609.899–5613.477	6126.884–6129.366	6530.712–6530.929
4498.640–4499.288	4563.146–4564.076	5100.539–5100.757	5613.808–5616.797	6129.802–6130.990	6531.200–6531.804
4499.422–4499.846	4564.260–4564.421	5101.011–5101.606	5617.789–5621.024	6131.454–6135.129	6532.052–6532.184
4500.215–4501.377	4564.640–4565.974	5101.916–5104.571	5621.453–5625.453	6135.293–6135.518	6532.664–6533.020
4502.104–4502.350	4566.365–4567.918	5104.739–5104.962	5627.414–5631.505	6135.922–6138.042	6533.261–6533.331
4502.507–4502.697	4568.517–4569.807	5105.254–5105.844	5632.125–5637.237	6139.136–6139.492	6533.586–6534.098
4503.637–4504.342	4570.153–4570.580	5106.105–5107.813	5637.911–5639.934	6139.903–6141.676	6534.408–6534.493
4504.790–4504.947	4570.741–4572.505	5108.248–5108.708	5640.252–5640.403	6141.779–6148.506	6534.734–6534.850
4506.683–4506.918	4573.048–4573.498	5109.000–5113.649	5640.638–5644.453	6149.089–6149.460	6535.284–6535.928
4507.053–4507.300	4573.913–4574.352	5113.948–5114.385	5644.765–5648.889	6149.632–6153.129	6536.037–6536.324
4508.152–4508.443	4574.583–4575.253	5115.064–5117.333	5649.216–5653.301	6153.486–6154.167	6536.851–6537.022
4509.172–4509.890	4575.692–4575.900	5117.508–5117.645	5653.743–5653.971	6154.298–6156.141	6537.565–6537.775
4510.743–4510.912	4576.131–4576.593	5117.795–5124.717	5654.855–5655.639	6156.616–6157.002	6538.100–6540.306
4511.777–4511.990	4577.090–4577.275	5124.986–5125.550	5655.815–5663.368	6157.525–6157.862	6540.577–6541.137
4512.158–4512.417	4577.379–4579.449	5125.762–5126.564	5663.911–5666.839	6158.055–6158.365	6541.455–6542.054
4512.653–4513.114	4579.970–4580.676	5127.096–5131.100	5667.100–5671.172	6159.164–6160.080	6542.434–6542.862
4514.047–4514.575	4580.989–4581.730	5131.345–5134.043	5672.008–5672.621	6160.514–6160.679	6543.111–6543.367
4515.047–4515.475	4582.726–4584.175	5135.362–5136.173	5672.897–5673.288	6160.845–6162.086	6544.153–6544.619
4516.195–4516.398	4584.500–4587.285	5136.355–5140.651	5673.533–5674.016	6162.279–6163.706	6545.093–6545.545
4517.422–4517.681	4587.912–4588.481	5141.041–5144.103	5677.178–5679.466	6163.810–6164.458	6545.872–6546.868
4517.906–4518.807	4820.119–4820.667	5144.500–5146.891	5679.835–5680.373	6164.865–6165.700	6547.015–6547.210
4519.371–4520.374	4820.905–4821.397	5147.295–5150.244	5681.980–5682.872	6166.094–6166.405	6548.214–6548.456
4522.574–4523.545	4823.187–4824.351	5150.446–5151.324	5684.050–5684.681	6166.494–6167.634	6548.751–6548.860
4523.850–4523.996	4825.815–4826.259	5151.678–5153.721	5686.421–5687.184	6167.993–6168.981	6549.211–6550.068
4524.516–4524.787	4828.851–4829.496	5153.981–5155.918	5687.823–5688.425	6169.105–6169.499	6550.442–6550.800
4525.035–4525.431	4831.002–4831.308	5156.196–5156.462	5689.234–5689.535	6169.645–6169.845	6550.987–6551.938
4525.736–4527.522	4831.536–4831.736	5157.457–5159.536	5689.689–5690.136	6170.114–6171.124	6552.109–6552.297
4527.737–4527.862	4832.309–4832.882	5159.669–5160.659	5690.337–5690.668	6171.324–6171.746	6552.866–6553.645
4528.212–4529.220	4833.038–4833.288	5160.932–5162.461	5691.100–5692.135	6171.968–6172.341	6554.028–6554.995
4530.397–4531.768	4834.897–4835.125	5163.274–5165.529	5694.435–5695.123	6172.819–6173.490	6555.206–6555.713
4533.117–4533.445	4835.777–4836.395	5165.714–5166.025	5695.996–5696.499	6173.739–6177.818	6555.931–6557.032
4533.820–4536.668	4836.724–4836.947	5166.165–5167.252	5697.117–5698.099	6179.267–6180.334	6557.336–6557.992
4537.316–4537.770	4837.549–4838.759	5167.424–5168.022	5698.254–5698.625	6180.612–6181.403	6558.687–6560.382
4538.520–4539.009	4839.406–4842.063	5168.506–5172.582	5699.832–5700.622	6182.867–6183.374	6561.195–6561.500
4539.498–4539.907	4842.560–4845.746	5172.798–5174.163	5700.823–5701.729	6183.783–6185.429	6564.339–6568.645
4540.601–4541.136	4847.890–4848.349	5174.781–5175.132	6099.997–6100.504	6186.527–6188.293	6568.927–6570.440
4541.420–4541.602	4848.791–4849.284	5175.324–5178.893	6101.693–6102.667	6188.724–6189.266	6571.059–6571.867
4542.319–4542.809	4851.391–4851.604	5179.059–5180.996	6102.795–6103.796	6189.795–6192.071	6572.306–6572.479
4543.355–4544.859	4852.412–4853.394	5182.160–5183.478	6104.155–6104.730	6192.356–6193.087	6572.643–6574.652
4545.030–4545.498	4854.707–4854.999	5183.753–5187.122	6104.953–6105.231	6193.965–6194.153	6574.942–6575.225
4545.851–4546.079	4855.274–4856.572	5187.346–5189.046	6105.454–6106.280	6194.341–6196.007	6575.405–6576.112
4546.364–4547.984	4857.240–4857.639	5189.296–5189.706	6106.917–6107.844	6196.258–6199.990	6576.505–6576.803
4548.658–4548.875	4858.921–4860.125	5189.905–5191.664	6107.987–6108.380	6520.359–6521.702	6577.039–6579.082
4549.343–4549.926	4863.312–4865.285	5191.914–5193.636	6109.220–6110.176	6523.000–6523.217	6579.475–6579.781